J. Phys. B: At. Mol. Opt. Phys. **42** (2009) 225002 (12pp) doi:10.1088/0953-4075/42/22/225002

R-matrix inner-shell electron-impact excitation of the Na-like iso-electronic sequence

G Y Liang, A D Whiteford and N R Badnell

Department of Physics, University of Strathclyde, Glasgow, G4 0NG, UK

E-mail: guiyun.liang@strath.ac.uk

Received 23 July 2009, in final form 17 September 2009
Published 5 November 2009
Online at stacks.iop.org/JPhysB/42/225002

Abstract

We present results for the inner-shell electron-impact excitation of all Na-like ions from Mg^{+} to Kr^{25+} obtained using the intermediate-coupling frame transformation *R*-matrix method with both Auger and radiation damping included via the optical potential approach. For each ion, the target and close-coupling expansions are taken to be the 59 LS terms (134 levels) belonging to configurations $2s^22p^63l$, $2s^22p^53s3l$ ($l \in$ s, p, d), $2s^22p^53p^2$ and $2s^22p^53p3d$. Radial wavefunctions were obtained using AUTOSTRUCTURE. Effective collision strengths are presented at temperatures ranging from $2 \times 10^2(q+1)^2$ K to $2 \times 10^6(q+1)^2$ K (where q is the residual charge of ions, i.e. $Z - 11$). Comparisons for the collision strengths and effective collision strengths are made with the results of other calculations for several ions which span the sequence. The Auger and radiation damping effects along the sequence have also been explored and their importance is highlighted. We further examine iso-electronic trends of both low- and high-temperature effective collision strengths.

1. Introduction

Emission lines arising from inner-shell transitions in sodium-like ions have been detected in many astrophysical objects (see, e.g., line lists of Behar *et al* [1] for Capella). Also, Jupén *et al* [2] have experimentally investigated core excitations in S^{5+}, Cl^{6+}, Ar^{7+} and Ti^{11+} by a beam-foil method and identified many inner-shell excitation lines. The most frequently investigated spectra in Na-like ions is that of Fe^{15+} due to the large cosmic abundance of Fe. A long-standing discrepancy between theory and astrophysical observation for two close $2p^53d\,^1P_1, {}^3D_1 \rightarrow 2p^6\,{}^1S_0$ transition lines of Fe^{16+}, at 15.01 and 15.26 Å, was found to be due to blending from the inner-shell transition line $2p^53s3d\,^2D_{3/2} \rightarrow 2p^63s^2S_{1/2}$ of Fe^{15+} at 15.256 Å (see the work of Brown *et al* [3]). Many high-resolution spectrometers on running and planned space satellites as well as on fusion devices make a large amount of high-resolution spectra available. To reliably model these features and hence interpret the properties of astrophysical objects, accurate atomic data are required. This provides a need for a large set of accurate baseline atomic data (see, e.g., [4, 5]).

Using relativistic many-body perturbation theory, Safronova *et al* [6, 7] reported the level energies of the core-excited levels from the $2s^22p^53l3l'$ and $2s2p^63l3l'$ configurations and the radiative decay rates from those levels to $2s^22p^63l''$ states of the Na-like ions with nuclear charge ranging from $Z = 14$ to $Z = 100$. An earlier comprehensive calculation of electron-impact excitation was the distorted-wave (DW) calculation of [8] for 10 Na-like ions with nuclear charge in the range $22 \leqslant Z \leqslant 62$. The earliest published *R*-matrix calculation (to our knowledge) is the work of Henry and Msezane [9], in which they analyse the contributions to the total ionization cross-section resulting from inner-shell excitation–autoionization for the ions Al^{2+} and Si^{3+} which are also addressed in this paper. For Fe^{15+}, Tayal and Henry [10] investigated the contributions from indirect-ionization processes (inner-shell excitation–autoionization and resonant-excitation double-autoionization) to the electron-impact ionization process using the close-coupling approach. Aggarwal and Keenan [11] performed a 134 level-resolved Dirac atomic *R*-matrix code (DARC) calculation with target expansion of configurations $2p^63l$, $2p^53s^2$, $2p^53s3p$, $2p^53s3d$, $2p^53p^2$ and $2p^53p3d$. Liang *et al* [12] calculated the excitations of Fe^{15+} with the intermediate-coupling frame transformation

(ICFT) *R*-matrix approach taking the Auger and radiation damping effects into account, and found the undamped *R*-matrix excitation data are significantly overestimated for many transitions, and up to a factor of 3 for some.

Because of the advantages (high accuracy and less-time demanding) of the ICFT *R*-matrix codes and high capability of parallel computer clusters, it is now feasible to provide the excitation data for iso-electronic sequences across the entire range of astrophysical interest within an *R*-matrix framework. Witthoeft *et al* [13] investigated the physics of electron-impact excitation along the F-like iso-electronic sequence (Ne^+ to Kr^{27+}) and Liang *et al* [14] also did an entire sequence calculation for the outer-shell excitation of Na-like ions. Based upon the robustness of the current suite of *R*-matrix codes, the *R*-matrix calculation of effective collision strengths currently can be performed automatically for each ion without manual intervention along an iso-electronic sequence after sufficiently accurate radial wavefunctions have been obtained. This ensures that each calculation is performed uniformly and reliably. Careful analysis of the results is still necessary so as to further validate the accuracy of the data along the sequence.

In this work, we study the inner-shell electron-impact excitation of the Na-like iso-electronic sequence (from Mg^+ to Kr^{25+}) via the ICFT *R*-matrix approach with Auger and radiation damping effects taken into account. In section 2, we discuss details of the calculation method and pay particular attention to comparing our underlying atomic structure with those of previous calculations. The excitation results themselves are discussed in section 3. Our work is a part of ongoing collaborative work—the UK Atomic Processes for Astrophysical Plasmas (APAP) network[1], a broadening of scope of the original UK RmaX network.

2. Sequence calculation

The aim of this work is to perform *R*-matrix calculations employing the intermediate-coupling frame transformation (ICFT) method (see [15]) for all Na-like ions from Mg^+ to Kr^{25+}. The details of the calculation for each ion follow closely those in the work of Liang *et al* [12] for Fe^{15+}. In our calculations, we included the following configuration basis set: $2s^22p^63l$, $2s^22p^53s3l$ ($l \in$ s, p, d), $2s^22p^53p^2$ and $2s^22p^53p3d$ in both the target and close-coupling expansions. This results in 59 LS terms and 134 fine-structure levels. In order to provide a self-consistent and complete database, we performed separate outer-shell excitations for all ions (Mg^+–Kr^{25+}) of the Na-like iso-electronic sequence; see [14] for details of this work.

2.1. Structure: levels

The orbital basis functions (1s–3d) were obtained from AUTOSTRUCTURE [16] using the Thomas–Femi–Dirac–Amaldi model potential. Relativistic effects were included perturbatively from the one-body Breit–Pauli operator (namely mass-velocity, spin–orbit and Darwin) without valence electron two-body fine-structure operators. This is consistent with the terms included in the standard *R*-matrix suite of codes. The radial scaling parameters, λ_{nl}, were obtained separately for each ion by a two-step optimization procedure (referred to as 'A' for the subsequent discussion). In the first step, the average energy of the terms in the $2p^63l$ configuration was optimized by allowing the λ_{1s}, λ_{2s} and λ_{2p} scaling parameters to change. Then, the average energy of the remaining 56 terms was minimized by optimizing the λ_{3l} scaling parameters. The resultant scaling parameters are listed in table 1. A test optimization (referred to as 'B' for the subsequent discussion) by minimizing the weighted sum of energies of all 59 LS terms was found to be worse than the two-step procedure, based upon the following three criteria: (1) the ratio between the weighted oscillator strength in velocity form (gf_V) and that in length form gf_L should be close to unity, (2) the resulted level energies should be in agreement with available experimental values and (3) the radiative decay rates should be consistent with previous published calculations. This assessment of the alternative optimizations is discussed throughout this section where appropriate. In the case of Ti^{11+}, the percentage of dipole transitions (to the five lowest-lying levels) with $|1.0 - gf_V/gf_L| \leqslant 20\%$ is about 80% and 57%, for calculations with optimization A and B, respectively (see figure 1).

There is significant level-mixing (see, e.g., table 1 of [17] for Fe^{15+}), which subsequently leads to different level ordering for different ions along the sequence. In their study of electron-impact excitation trends along the fluorine isoelectronic sequence, Witthoeft *et al* [13] also reported such non-continuity along the sequence. Hence, caution should be taken when investigating trends along an iso-electronic

Table 1. Radial scaling factors used in AUTOSTRUCTURE to minimize the total energies of $2s^22p^63l$ (1s, 2s and 2p orbitals) and $2s^22p^53l3l'$ ($3l$ orbitals), respectively.

Ion	1s	2s	2p	3s	3p	3d
Mg	1.477 00	1.045 70	0.998 44	1.126 27	1.109 34	1.140 79
Al	1.463 35	1.052 39	1.003 90	1.123 57	1.106 07	1.139 47
Si	1.453 47	1.057 74	1.007 84	1.129 35	1.103 73	1.133 78
P	1.444 38	1.062 48	1.010 80	1.133 97	1.103 59	1.133 34
S	1.436 49	1.066 49	1.013 11	1.137 78	1.104 30	1.134 76
Cl	1.429 73	1.069 90	1.014 99	1.140 95	1.105 31	1.136 75
Ar	1.423 69	1.072 88	1.016 54	1.143 66	1.106 44	1.138 85
K	1.418 72	1.074 88	1.017 87	1.146 32	1.107 71	1.140 76
Ca	1.413 62	1.077 68	1.018 96	1.147 94	1.108 62	1.142 75
Sc	1.409 35	1.079 65	1.019 93	1.149 70	1.109 63	1.144 47
Ti	1.405 76	1.081 43	1.020 79	1.151 21	1.110 57	1.146 04
V	1.402 30	1.082 99	1.021 56	1.152 57	1.111 45	1.147 46
Cr	1.399 19	1.084 41	1.022 24	1.153 79	1.112 26	1.148 75
Mn	1.396 25	1.085 69	1.022 85	1.154 89	1.113 01	1.149 93
Fe	1.393 64	1.086 86	1.023 41	1.155 88	1.113 71	1.151 00
Co	1.391 23	1.087 92	1.023 91	1.156 78	1.114 36	1.151 98
Ni	1.389 14	1.088 90	1.024 37	1.157 61	1.114 96	1.152 88
Cu	1.387 07	1.089 79	1.024 80	1.158 36	1.115 53	1.153 71
Zn	1.385 16	1.090 62	1.025 19	1.159 05	1.116 05	1.154 47
Ga	1.383 37	1.091 38	1.025 55	1.159 69	1.116 54	1.155 18
Ge	1.381 65	1.092 09	1.025 88	1.160 28	1.117 00	1.155 83
As	1.380 11	1.092 75	1.026 20	1.160 83	1.117 43	1.156 44
Se	1.378 55	1.093 36	1.026 49	1.161 34	1.117 84	1.157 00
Br	1.377 20	1.093 94	1.026 76	1.161 81	1.118 20	1.157 54
Kr	1.375 91	1.094 47	1.027 03	1.162 27	1.118 56	1.158 03

[1] http://www.apap-network.org.

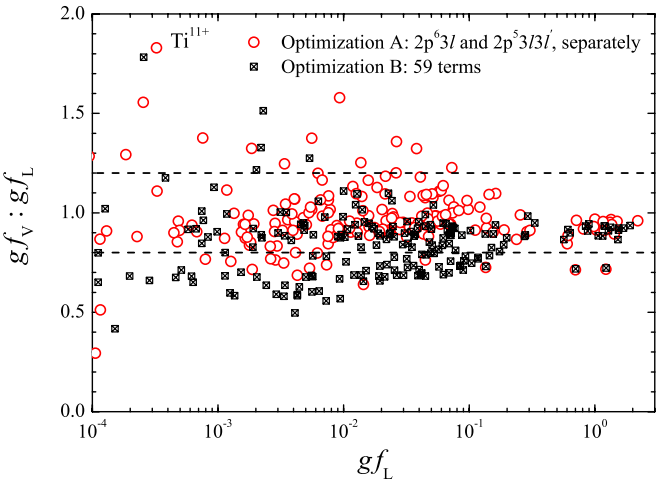

Figure 1. The ratio gf_V/gf_L of weighted oscillator strengths between the velocity gf_V and length gf_L forms, as a function of the length form, for Ti^{11+}. Optimization A represents the two-step optimizations to obtain the scaling parameters, while optimization B refers to our test minimization of the average energy of all 59 terms. The horizontal dashed lines correspond to agreement within 20%.

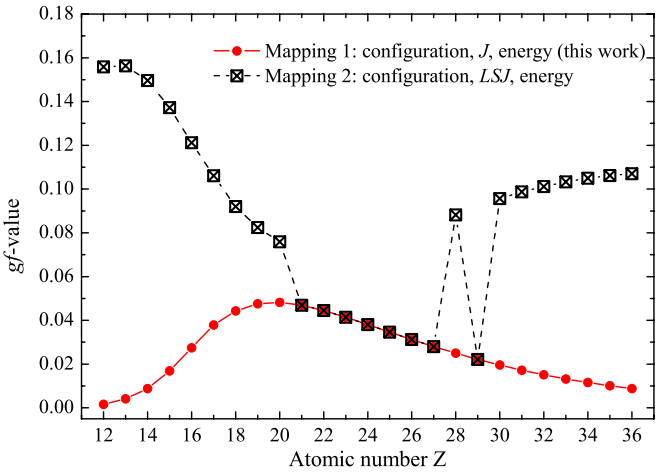

Figure 2. gf-values along the sequence for the $2p^5 3s3p\ J = 3/2 \rightarrow 2p^6 3p\ J = 1/2$ (14–2) transition under two different level mappings. The level mapping is relative to that of Fe^{15+}.

sequence. In this work, we eliminate uncertainty originating from the non-continuity of level-ordering along the sequence by using different level mapping procedures. We first consider the weighted oscillator strengths (gf-value) as a function of nuclear charge, Z, figure 2 reveals that configuration, total angular momentum J and energy ordering are the best choice as 'good' quantum numbers[2] over the iso-electronic sequence, that convention is adopted throughout this paper unless otherwise specified.

The resulting energies along the sequence are displayed in figure 3(a), in which they have been scaled by a factor of $1/(q+1)^2$ (where $q = Z - 11$ for the Na-like sequence), as well as listed in table 2 for 13 ions spanning Mg^+ to Kr^{25+}. In table 2, we present the level specifications by

[2] We note, of course, that configuration is technically not a good quantum number but analysis shows that it behaves as that for the present data.

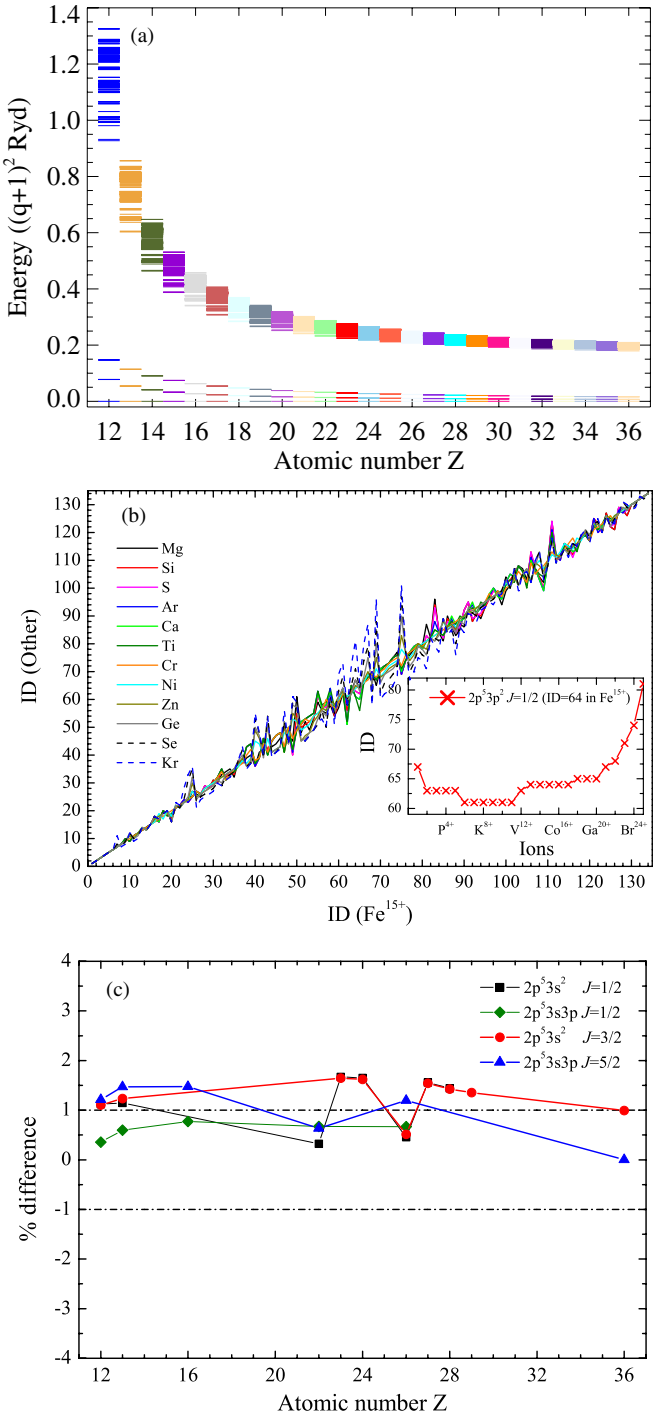

Figure 3. Energy levels (mapped as shown in figure 2) of all ions along the sequence. (a) The present theoretical energies in unit of $(q+1)^2$ Ryd (where q is the residual nuclear charge); (b) the level ordering with the original level index (ID) relative to the ordering of Fe^{15+} by mapping according to the good quantum number—configuration, total angular momentum J and energy ordering for ions spanning the entire sequence. The inset shows the trace of the $2p^5 3p^2\ J = 1/2$ level (ID = 64 in Fe^{15+}) along the Na iso-electronic sequence; (c) comparison with available observed energies listed in NIST v.3 for several core-excited states.

configurations and LSJ states for convenience although, as discussed above, they are not good quantum numbers for highly charged ions. The level energies listed in table 2

Table 2. Part of energy levels (Ryd) for ions over the sequence. The level index and specification correspond to the level ordering in Fe^{15+}.

ID	Levels	Mg	Si	S	Ar	Ca	Ti	Cr
01	$2s^22p^63s\ ^2S_{1/2}$	0.0000	0.0000	0.0000	0.0000	0.0000	0.0000	0.0000
02	$2s^22p^63p\ ^2P_{1/2}$	0.3104	0.6512	0.9715	1.2869	1.6002	1.9132	2.2269
03	$2s^22p^63p\ ^2P_{3/2}$	0.3122	0.6573	0.9859	1.3159	1.6523	1.9993	2.3612
04	$2s^22p^63d\ ^2D_{3/2}$	0.5884	1.4493	2.2633	3.0524	3.8317	4.6121	5.4013
05	$2s^22p^63d\ ^2D_{5/2}$	0.5884	1.4496	2.2648	3.0563	3.8401	4.6278	5.4280
06	$2s^22p^53s^2\ ^2P_{3/2}$	3.7091	7.4122	12.2232	18.1425	25.1690	33.3012	42.5377
07	$2s^22p^53s^2\ ^2P_{1/2}$	3.7275	7.4550	12.3090	18.2972	25.4273	33.7080	43.1491
08	$2s^22p^53s3p\ ^4S_{3/2}$	3.9233	7.8179	12.8264	18.9522	26.1945	34.5518	44.0220
09	$2s^22p^53s3p\ ^4D_{5/2}$	3.9758	7.9137	12.9608	19.1204	26.3914	34.7726	44.2627
10	$2s^22p^53s3p\ ^4D_{7/2}$	3.9709	7.9045	12.9472	19.1044	26.3779	34.7694	44.2808
11	$2s^22p^53s3p\ ^4D_{3/2}$	3.9804	7.9237	12.9789	19.1485	26.4299	34.8204	44.3182
12	$2s^22p^53s3p\ ^2P_{1/2}$	3.9840[$^4D_{1/2}$]	7.9325[$^4D_{1/2}$]	12.9980[$^4D_{1/2}$]	19.1846[$^4D_{1/2}$]	26.4882[$^4D_{1/2}$]	34.9027[$^4D_{1/2}$]	44.4238
13	$2s^22p^53s3p\ ^4P_{5/2}$	4.0087	7.9745	13.0481	19.2358	26.5394	34.9606	44.5014
14	$2s^22p^53s3p\ ^2D_{3/2}$	4.0137[$^4P_{3/2}$]	7.9852[$^4P_{3/2}$]	13.0656[$^4P_{3/2}$]	19.2577[$^4P_{3/2}$]	26.5620[$^4P_{3/2}$]	34.9802	44.5144
15	$2s^22p^53s3p\ ^2S_{1/2}$	4.0160[$^4P_{1/2}$]	7.9907[$^4P_{1/2}$]	13.0793[$^4P_{1/2}$]	19.2909[$^4P_{1/2}$]	26.6301[$^4P_{1/2}$]	35.0946[$^4P_{1/2}$]	44.6760[$^4P_{1/2}$]
16	$2s^22p^53s3p\ ^4D_{1/2}$	4.0469[$^2P_{1/2}$]	8.0356[$^2P_{1/2}$]	13.1362[$^2P_{1/2}$]	19.3582[$^2P_{1/2}$]	26.7102[$^2P_{1/2}$]	35.2073[$^2P_{1/2}$]	44.8696
17	$2s^22p^53s3p\ ^2P_{3/2}$	4.0347[$^2D_{3/2}$]	8.0129[$^2D_{3/2}$]	13.1078[$^2D_{3/2}$]	19.3361[$^2D_{3/2}$]	26.7102[$^2D_{3/2}$]	35.2406[$^4P_{3/2}$]	44.9369
18	$2s^22p^53s3p\ ^4P_{1/2}$	4.1240[$^2S_{1/2}$]	8.1304[$^2S_{1/2}$]	13.2487[$^2S_{1/2}$]	19.4888[$^2S_{1/2}$]	26.8595[$^2S_{1/2}$]	35.3706[$^2S_{1/2}$]	45.0307[$^2S_{1/2}$]
19	$2s^22p^53s3p\ ^4P_{3/2}$	4.0509[$^2P_{3/2}$]	8.0458[$^2P_{3/2}$]	13.1584[$^2P_{3/2}$]	19.4015[$^2P_{3/2}$]	26.7865[$^2P_{3/2}$]	35.3271[$^2P_{3/2}$]	45.0392
20	$2s^22p^53s3p\ ^2D_{5/2}$	4.0416	8.0300	13.1403	19.3871	26.7825	35.3394	45.0711
21	$2s^22p^53s3p\ ^2D_{5/2}$	4.2316	8.2938	13.4619	19.7400	27.1297	35.6328	45.2521
22	$2s^22p^53s3p\ ^2P_{3/2}$	4.2434[$^2D_{3/2}$]	8.3176[$^2D_{3/2}$]	13.5009[$^2D_{3/2}$]	19.7953	27.2016	35.7213	45.3569
23	$2s^22p^53s3p\ ^2P_{1/2}$	4.2659	8.3609	13.5760	19.9199	27.4005	36.0276	45.8122
24	$2s^22p^53s3p\ ^2D_{3/2}$	4.2604[$^2P_{3/2}$]	8.3514[$^2P_{3/2}$]	13.5653[$^2P_{3/2}$]	19.9144	27.4099	36.0637	45.8890
25	$2s^22p^53s3p\ ^2S_{1/2}$	4.4000	8.6366	13.9698	20.4153	27.9828	36.6825	46.5267
26	$2s^22p^53p^2\ ^4P_{3/2}$	4.3993[$^2P_{3/2}$]	8.6621[$^2P_{3/2}$]	14.0266[$^2P_{3/2}$]	20.5029[$^2P_{3/2}$]	28.0935[$^2P_{3/2}$]	36.7997[$^2P_{3/2}$]	46.6221[$^2P_{3/2}$]
27	$2s^22p^53p^2\ ^2P_{1/2}$	4.3937	8.6507	14.0088	20.4804	28.0697	36.7797	46.6130
28	$2s^22p^53p^2\ ^4P_{5/2}$	4.4118[$^2F_{5/2}$]	8.6944	14.0547	20.5291	28.1215	36.8342	46.6695
29	$2s^22p^53p^2\ ^2F_{7/2}$	4.4008	8.6764	14.0526	20.5407	28.1443	36.8657	46.7075
30	$2s^22p^53p^2\ ^2P_{3/2}$	4.4365[$^2D_{3/2}$]	8.7044[$^4P_{3/2}$]	14.0745[$^4P_{3/2}$]	20.5639[$^4P_{3/2}$]	28.1747[$^4P_{3/2}$]	36.9063[$^4P_{3/2}$]	46.7575[$^4P_{3/2}$]
31	$2s^22p^53p^2\ ^2D_{5/2}$	4.4328	8.7028[$^2F_{5/2}$]	14.1004[$^2F_{5/2}$]	20.6151[$^2F_{5/2}$]	28.2492[$^2F_{5/2}$]	37.0045	46.8795
32	$2s^22p^53p^2\ ^2D_{3/2}$	4.4417[$^4P_{3/2}$]	8.7577	14.1664[$^4D_{3/2}$]	20.6790[$^4D_{3/2}$]	28.3056	37.0479	46.9084
33	$2s^22p^53p^2\ ^4P_{1/2}$	4.4446	8.7110	14.0871	20.5860	28.2132	36.9721	46.8658
34	$2s^22p^53p^2\ ^4D_{7/2}$	4.4690	8.7526	14.1386	20.6401	28.2638	37.0152	46.9002
35	$2s^22p^53p^2\ ^4D_{5/2}$	4.4372[$^4P_{5/2}$]	8.7515[$^2D_{5/2}$]	14.1547	20.6627	28.2893	37.0386	46.9198
36	$2s^22p^53p^2\ ^4D_{1/2}$	4.4829	8.7836	14.1983	20.7440	28.4296	37.2607	47.2383
37	$2s^22p^53p^2\ ^4S_{3/2}$	4.4789[$^4D_{3/2}$]	8.7750[$^4D_{3/2}$]	14.1965[$^2D_{3/2}$]	20.7579[$^2D_{3/2}$]	28.4644[$^2D_{3/2}$]	37.3230[$^2D_{3/2}$]	47.3091[$^2D_{3/2}$]

for each ion are consistent with the level mapping procedure mentioned above, and they are followed by their LSJ states in the case of being different from that of Fe^{15+}. Comparisons in a later discussion are based on this level mapping. The mapping procedure was performed using RAP (*R*-matrix Analysis Package[3]) developed specifically to analyse the large amount of excitation data produced from calculations along an iso-electronic sequence. The level ordering with the original level index (ID) for each ion relative to that in Fe^{15+} after this mapping—configurations, *J* and energy ordering—is shown in figure 3(b). It clearly indicates that there are significant level-crossing interaction effects for the core-excited states along the sequence. For example, the 64th level ($2p^53p^2$ $J = 1/2$) in Fe^{15+} moves to the 74th level in Br^{24+} as shown by the inset in figure 3(b).

In order to maintain consistency and so as not to introduce arbitrary changes along the sequence, we performed the optimization procedure automatically in AUTOSTRUCTURE without any manual readjustment. Comparison with available limited experimental values from NIST [18] in figure 3(c) reveals that present theoretical energies are typically accurate to within 1.5% over the sequence—even for lower charged ions ($Z < 16$). The calculation based upon the present two-step optimization A shows a much better agreement compared to our test optimization B. In the latter case, the difference can be up to 7% for the $2s^22p^53s^2$ $J = 3/2$ level of Mg^+ when compared with NIST data (for clarity, this has not been plotted in figure 3(c)).

2.2. Structure: A-values

A further test of our structure calculations is to compare radiative decay rates ($A_{i,j}$ for a given $i \rightarrow j$ transition) with those of other calculations. In figure 4, we compare our present AUTOSTRUCTURE calculation with those of [7][4] along the sequence, for transition rates from core-excited states of $2p^53s3p$ $J = 1/2$ (12th) in figure 4(a); $2p^53s3p$ $J = 1/2$ (15th) in (b); $2p^53s3p$ $J = 1/2$ (16th) in (c) and $2p^53s3p$ $J =$

[3] http://www.apap-network.org/RAP.

[4] The data are sampled from figure 2 in their work and as such have an intrinsic uncertainty associated with sampling from the figure.

Table 2. (Continued.)

ID	Levels	Fe	Ni	Zn	Ge	Se	Kr
01	$2s^22p^63s\,^2S_{1/2}$	0.0000	0.0000	0.0000	0.0000	0.0000	0.0000
02	$2s^22p^63p\,^2P_{1/2}$	2.5424	2.8604	3.1818	3.5077	3.8391	4.1772
03	$2s^22p^63p\,^2P_{3/2}$	2.7421	3.1465	3.5790	4.0447	4.5489	5.0976
04	$2s^22p^63d\,^2D_{3/2}$	6.2059	7.0319	7.8850	8.7711	9.6959	10.6657
05	$2s^22p^63d\,^2D_{5/2}$	6.2485	7.0963	7.9785	8.9023	9.8752	10.9051
06	$2s^22p^53s^2\,^2P_{3/2}$	52.8771	64.3179	76.8585	90.4975	105.2335	121.0650
07	$2s^22p^53s^2\,^2P_{1/2}$	53.7620	65.5590	78.5536	92.7610	108.1972	124.8801
08	$2s^22p^53s3p\,^4S_{3/2}$	54.6025	66.2909	79.0842	92.9796	107.9745	124.0668
09	$2s^22p^53s3p\,^4D_{5/2}$	54.8608	66.5656	79.3759	93.2902	108.3069	124.4244
10	$2s^22p^53s3p\,^4D_{7/2}$	54.9143	66.6725	79.5583	93.5750	108.7263	125.0166
11	$2s^22p^53s3p\,^4D_{3/2}$	54.9223	66.6317[$^2D_{3/2}$]	79.4456[$^2D_{3/2}$]	93.3633[$^2D_{3/2}$]	108.3837[$^2D_{3/2}$]	124.5056[$^2D_{3/2}$]
12	$2s^22p^53s3p\,^2P_{1/2}$	55.0498	66.7793	79.6108	93.5431	108.5745	124.7037
13	$2s^22p^53s3p\,^4P_{5/2}$	55.1640	66.9510	79.8655	93.9107	109.0905	125.4091
14	$2s^22p^53s3p\,^2D_{3/2}$	55.1672	66.9413[$^4P_{3/2}$]	79.8401[$^2P_{3/2}$]	93.8676[$^2P_{3/2}$]	109.0282[$^2P_{3/2}$]	125.3270[$^2P_{3/2}$]
15	$2s^22p^53s3p\,^2S_{1/2}$	55.3735	67.1909	80.1326	94.2032	109.4071	125.7491
16	$2s^22p^53s3p\,^4D_{1/2}$	55.7109	67.7419	80.9291[$^4P_{1/2}$]	95.1916[$^4P_{1/2}$]	110.5937[$^4P_{1/2}$]	127.1332[$^4P_{1/2}$]
17	$2s^22p^53s3p\,^2P_{3/2}$	55.8086	67.8625[$^4D_{3/2}$]	80.9556	95.0815	110.3336	126.7202
18	$2s^22p^53s3p\,^4P_{1/2}$	55.8443	67.8117	80.9751[$^4D_{1/2}$]	95.4242[$^4D_{1/2}$]	111.1054[$^4D_{1/2}$]	128.0363[$^4D_{1/2}$]
19	$2s^22p^53s3p\,^4P_{3/2}$	55.9384	67.9665[$^2P_{3/2}$]	81.1420[$^4D_{3/2}$]	95.6184[$^4D_{3/2}$]	111.3319[$^4D_{3/2}$]	128.2979[$^4D_{3/2}$]
20	$2s^22p^53s3p\,^2D_{5/2}$	55.9649	67.8367	80.8161	94.9213	110.1571	126.5285
21	$2s^22p^53s3p\,^2D_{5/2}$	56.0178	68.1329	81.4891	96.0916	111.9613	129.1213
22	$2s^22p^53s3p\,^2P_{3/2}$	56.1137	68.0759	81.4033[$^4P_{3/2}$]	95.9879[$^4P_{3/2}$]	111.8415[$^4P_{3/2}$]	128.9865[$^4P_{3/2}$]
23	$2s^22p^53s3p\,^2P_{1/2}$	56.7670	68.9065	82.2473	96.8083	112.6097	129.6728
24	$2s^22p^53s3p\,^2D_{3/2}$	56.9008	69.1156	82.5514	97.2285	113.1687	130.3958
25	$2s^22p^53s3p\,^2S_{1/2}$	57.5308	69.7144	83.1011	97.7178	113.5932	130.7566
26	$2s^22p^53p^2\,^4P_{3/2}$	57.5603	69.6123	82.7745	97.0426	112.4124	128.8811
27	$2s^22p^53p^2\,^2P_{1/2}$	57.5722	69.6598	82.8784	97.2310	112.7211	129.3529
28	$2s^22p^53p^2\,^4P_{5/2}$	57.6293	69.7162	82.9326	97.2821	112.7681	129.3954
29	$2s^22p^53p^2\,^2F_{7/2}$	57.6721	69.7627	82.9824	97.3351	112.8248	129.4563
30	$2s^22p^53p^2\,^2P_{3/2}$	57.7283	69.8203	83.0370	97.3840	112.8672	129.4924
31	$2s^22p^53p^2\,^2D_{5/2}$	57.8726	69.9887	83.2330	97.6096	113.1230	129.7778
32	$2s^22p^53p^2\,^2D_{3/2}$	57.8902	69.9971	83.2330	97.6022	113.1088	129.7573
33	$2s^22p^53p^2\,^4P_{1/2}$	57.8977	70.0722	83.3944	97.8701	113.5037[$^2S_{1/2}$]	130.2978[$^2S_{1/2}$]
34	$2s^22p^53p^2\,^4D_{7/2}$	57.9252	70.0964	83.4207	97.9055	113.5584	130.3874
35	$2s^22p^53p^2\,^4D_{5/2}$	57.9436	70.1147	83.4390	97.9237	113.5768	130.4068
36	$2s^22p^53p^2\,^4D_{1/2}$	58.3600	70.6204	84.0256	98.5608	114.2360	131.0611
37	$2s^22p^53p^2\,^4S_{3/2}$	58.4290	70.6934	84.1186	98.6856	114.4100	131.2910

1/2 (18th) in (d) $\rightarrow 2p^63p\ J = 1/2$ (second) and $J = 3/2$ (third) levels. It shows that the present calculations are in good agreement with those of [7] except for ions in the region of large spikes and/or dips. We note that our spikes and/or dips along the sequence occur at places similar to those reported by Safronova *et al* [7]. Chen [19] has explained this particular issue along the sequence to be due to level-crossing interaction, relativistic terms and configuration interaction. At the points in question, a large difference being up to orders of magnitude was found, which is due to strong level mixing and the different methods adopted.

We make a further detailed comparison with the results of previous calculations (including the work of Safronova *et al* [7][5]) for four ions spanning the sequence: Si^{3+}, Ar^{7+}, Ti^{11+} and Zn^{19+}; see table 3. We also performed fully relativistic calculations with the Flexible Atomic Code (FAC) of [20] for these ions. For Si^{3+}, around 40% of transitions show agreement to within 25% between the present (i.e. AUTOSTRUCTURE using optimization strategy A) and FAC calculations as well as with those of [7] using first-order perturbation theory (only Si^{3+} using this method is shown here). However the test calculation with optimization B (not shown here) shows a better agreement with those of [7] with relativistic many-body perturbation theory (RMBPT). But the percentage of all dipole transitions to five lowest-lying levels with $|1.0 - gf_V/gf_L| \leqslant 20\%$ drops from 73% (optimization A) to 12% (optimization B). They are systematically higher than the present (i.e. optimization A). As discussed above, we use the optimization procedure (A) for the present calculations, which is confirmed to be the better optimization procedure for Na-like ions (see figure 1). For Ar^{7+}, 85% of all list transitions shows agreement with present FAC calculations to within 25%. Comparison with the results of [19] shows an agreement of ∼5%–50% (74% of transitions are within 25%). Good agreement (within 25%) appears when compared with the work of Safronova *et al* [7] for 63% of the listed transitions. Moreover, 75% of all dipole transitions to five lowest-lying levels shows an agreement of 20% between the velocity and length forms of the oscillator strength. For Ti^{11+}, 80% of transitions agree with FAC calculations to

[5] Tabulated radiative decay rates were obtained by private communication.

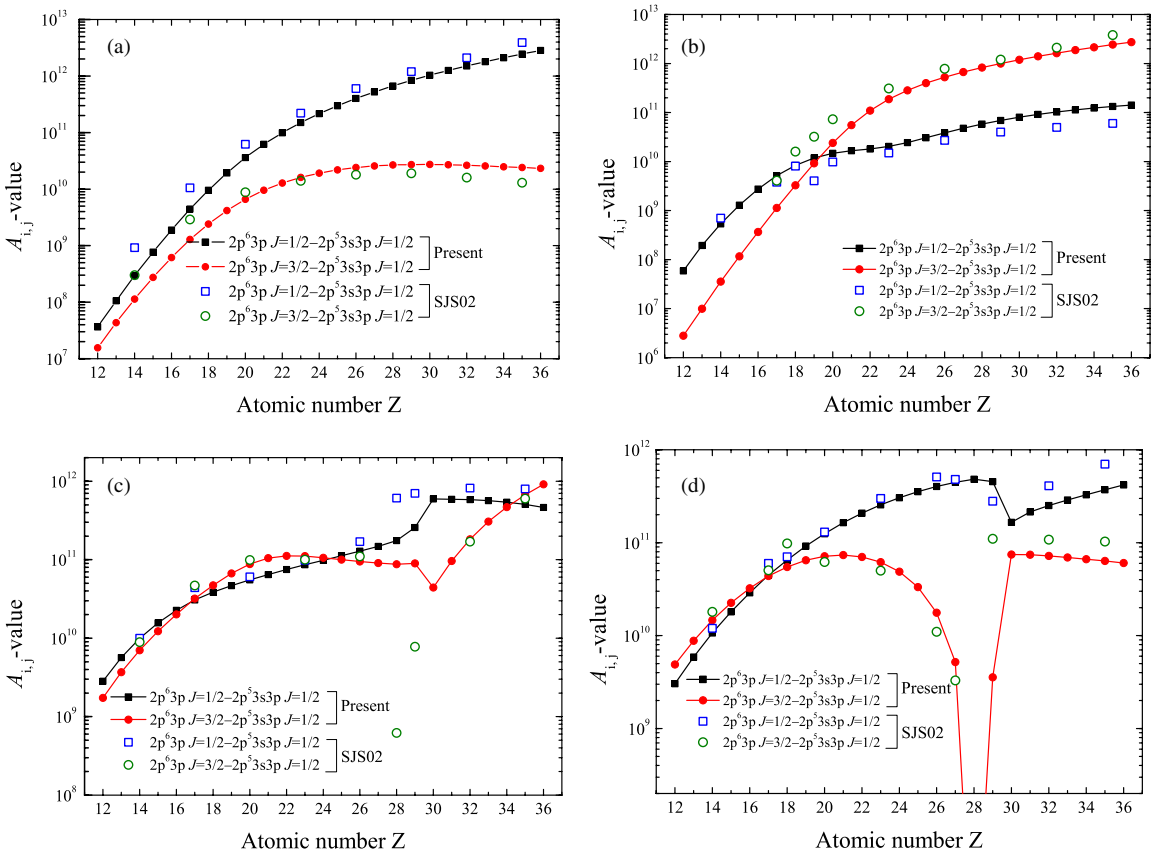

Figure 4. Comparison of $A_{i,j}$-values between the present AUTOSTRUCTURE calculation and previous relativistic many-body perturbation theory (RMBPT) calculation ([7], SJS02) as well as calculated FAC results along the sequence. (a) $2p^5 3s3p\ J = 1/2$ (12th) $\rightarrow$ $2p^6 3p\ J = 1/2$ (second) and $\rightarrow$ $2p^6 3p\ J = 3/2$ (third); (b) $2p^5 3s3p\ J = 1/2$ (15th) $\rightarrow$ $2p^6 3p\ J = 1/2$ (second) and $\rightarrow$ $2p^6 3p\ J = 3/2$ (third); (c) $2p^5 3s3p\ J = 1/2$ (16th) $\rightarrow$ $2p^6 3p\ J = 1/2$ (second) and $\rightarrow$ $2p^6 3p\ J = 3/2$ (third); (d) $2p^5 3s3p\ J = 1/2$ (18th) $\rightarrow$ $2p^6 3p\ J = 1/2$ (second) and $\rightarrow$ $2p^6 3p\ J = 3/2$ (third).

within 20%, and 60% of transitions show an agreement of within 10%. Comparison with the results of [19] also shows an agreement of 20% for 73% of transitions. The present AUTOSTRUCTURE calculations show a slightly worse agreement with the results of [8] and [7]. By contrast, the test AUTOSTRUCTURE calculation with optimization B (not listed in table 3) shows a better agreement with [8] and [7]. But the percentage of dipole transitions to the five lowest-lying levels with $|1.0 - gf_V/gf_L| \leqslant 20\%$ drops from 80% (optimization A) to 57% (optimization B). For Zn^{19+}, 75% of all listed transitions show agreement with FAC calculations to within 20%. As for Ti^{11+}, a slightly worse agreement with [8] and [7] also appears for Zn^{19+}. Unlike Ti^{11+}, there is a comparable percentage (optimization A: 74%; B: 77%) of the dipole transitions to the five lowest-lying levels with $|1.0 - gf_V/gf_L|$ less than 20%—as one would expect when moving to higher charge ions. We have shown that the present structure calculations (optimization A) for ions with nuclear charge $Z \gtrsim 18$ are reliable and, even for ions with $14 < Z < 18$, the radiative decay rates are accurate to 25%.

2.3. Scattering

For Fe^{15+}, Liang *et al* [12] demonstrated that the Auger and radiation damping effects significantly reduce the resonant enhancement of the excitation collision strengths for inner-shell transitions. This means previous *R*-matrix calculations which did not include such effects (e.g. [11]) significantly overestimate the effective collisions strengths. We take the Auger-plus-radiation damping effects into account via a complex optical potential as discussed in [21] and [22]. For clarity, we give a brief description of the two damping effects for the specific case of Na-like ions. Over the sequence Mg^+–Kr^{25+}, the resonance state configurations are of the form $[2s, 2p]^{m-1}[3s, 3p, 3d]^2 nl$ (here $m = 8$, $n \geqslant 3$), and they can decay via the following channels:

$$[2s, 2p]^{m-1}[3s, 3p, 3d]^2 nl \rightarrow [2s, 2p]^m [3s, 3p, 3d] + e^- \quad (1)$$

$$\rightarrow [2s, 2p]^m nl + e^- \quad (2)$$

$$\rightarrow [2s, 2p]^m [3s, 3p, 3d]^2 + h\nu \quad (3)$$

$$\rightarrow [2s, 2p]^m [3s, 3p, 3d] nl + h\nu. \quad (4)$$

The participator LM*n* Auger pathway (1) scales as n^{-3} and is automatically described in the *R*-matrix method by the contribution to the close-coupling expansion from the right-hand side of (1). However, the spectator LMM Auger pathway (2) is independent of n and only low-n resonances ($n \leqslant 3$

Table 3. Comparison of radiative rates (s^{-1}) of selected transitions for present and previous calculations.

		Si^{3+}					Ar^{7+}				
i–j	Transitions	Terms	Present	FAC	SJS02[a]	SJS02[b]	Terms	Present	FAC	Chen89[c]	SJS02
1–6	$2p^63s \leftarrow 2p^53s^2$	$^2S_{1/2}$–$^2P_{3/2}$	1.53(10)[e]	1.08(10)	1.66(10)	1.16(10)	$^2S_{1/2}$–$^2P_{3/2}$	8.60(10)	7.38(10)	6.94(10)	1.00(11)
1–7	$2p^63s \leftarrow 2p^53s^2$	$^2S_{1/2}$–$^2P_{1/2}$	1.51(10)	1.08(10)	1.65(10)	1.15(10)	$^2S_{1/2}$–$^2P_{1/2}$	8.43(10)	7.42(10)	6.99(10)	9.96(10)
1–38	$2p^63s \leftarrow 2p^53s3d$	$^2S_{1/2}$–$^4P_{1/2}$	1.25(08)	1.19(08)			$^2S_{1/2}$–$^4P_{1/2}$	1.52(09)	1.66(09)		
1–39	$2p^63s \leftarrow 2p^53s3d$	$^2S_{1/2}$–$^4P_{3/2}$	3.50(08)	3.26(08)	6.39(08)	5.54(08)	$^2S_{1/2}$–$^4P_{3/2}$	4.20(09)	4.65(09)		5.20(09)
1–53	$2p^63s \leftarrow 2p^53s3d$	$^2S_{1/2}$–$^4D_{1/2}$	5.32(09)	7.67(09)	6.89(09)	6.63(09)	$^2S_{1/2}$–$^4D_{1/2}$	1.15(11)	1.39(11)		1.76(11)
1–54	$2p^63s \leftarrow 2p^53s3d$	$^2S_{1/2}$–$^4D_{3/2}$	3.44(09)	5.24(09)	8.69(09)	7.64(09)	$^2S_{1/2}$–$^4D_{3/2}$	8.08(10)	1.09(11)		1.52(11)
2–8	$2p^63p \leftarrow 2p^53s3p$	$^2P_{1/2}$–$^4S_{3/2}$	9.93(06)	9.10(06)	2.15(07)	1.51(07)	$^2P_{1/2}$–$^4S_{3/2}$	1.69(08)	1.56(08)	1.58(08)	2.64(08)
2–11	$2p^63p \leftarrow 2p^53s3p$	$^2P_{1/2}$–$^4D_{3/2}$	7.86(08)	7.67(08)	1.88(09)	1.28(09)	$^2P_{1/2}$–$^4D_{3/2}$	1.67(10)	1.58(10)	1.54(10)	2.51(10)
2–12	$2p^63p \leftarrow 2p^53s3p$	$^2P_{1/2}$–$^4D_{1/2}$	2.94(08)	3.35(08)	9.61(08)	6.76(08)	$^2P_{1/2}$–$^4D_{1/2}$	9.57(09)	9.67(09)	1.14(10)	2.04(10)
2–14	$2p^63p \leftarrow 2p^53s3p$	$^2P_{1/2}$–$^4P_{3/2}$	9.55(08)	9.27(08)	2.96(09)	1.97(09)	$^2P_{1/2}$–$^4P_{3/2}$	2.87(10)	2.52(10)	2.16(10)	3.18(10)
2–15	$2p^63p \leftarrow 2p^53s3p$	$^2P_{1/2}$–$^4P_{1/2}$	5.36(08)	4.43(08)	7.60(08)	5.35(08)	$^2P_{1/2}$–$^4P_{1/2}$	8.34(09)	6.31(09)	5.77(09)	8.29(09)
2–16	$2p^63p \leftarrow 2p^53s3p$	$^2P_{1/2}$–$^2P_{1/2}$	9.94(09)	6.83(09)	1.04(10)	7.18(09)	$^2P_{1/2}$–$^2P_{1/2}$	3.86(10)	3.17(10)	2.62(10)	3.81(10)
2–17	$2p^63p \leftarrow 2p^53s3p$	$^2P_{1/2}$–$^2D_{3/2}$	1.63(10)	1.07(10)	1.38(10)	9.30(09)	$^2P_{1/2}$–$^2D_{3/2}$	6.02(10)	4.90(10)	4.09(10)	5.70(10)
2–19	$2p^63p \leftarrow 2p^53s3p$	$^2P_{1/2}$–$^2P_{3/2}$	4.54(09)	3.50(09)	5.61(09)	3.87(09)	$^2P_{1/2}$–$^2P_{3/2}$	2.17(10)	1.95(10)	1.90(10)	2.83(10)
2–22	$2p^63p \leftarrow 2p^53s3p$	$^2P_{1/2}$–$^2D_{3/2}$	8.63(09)	6.02(09)	9.86(09)	7.30(09)	$^2P_{1/2}$–$^2P_{3/2}$	4.25(10)	3.63(10)	4.03(10)	5.42(10)
2–23	$2p^63p \leftarrow 2p^53s3p$	$^2P_{1/2}$–$^2P_{1/2}$	8.22(09)	5.44(09)	1.32(10)	9.53(09)	$^2P_{1/2}$–$^2P_{1/2}$	3.61(10)	2.98(10)	2.97(10)	3.38(10)
3–83	$2p^63p \leftarrow 2p^53p3d$	$^2P_{3/2}$–$^4P_{1/2}$	8.59(08)	1.43(09)	1.57(09)	1.35(09)	$^2P_{3/2}$–$^4P_{1/2}$	8.38(09)	1.46(10)		9.00(09)
3–107	$2p^63p \leftarrow 2p^53p3d$	$^2P_{3/2}$–$^4D_{5/2}$	1.46(10)	2.88(09)	5.16(09)	4.32(09)	$^2P_{3/2}$–$^2D_{5/2}$	2.52(11)	3.23(11)		2.87(11)
3–120	$2p^63p \leftarrow 2p^53p3d$	$^2P_{3/2}$–$^4P_{3/2}$	9.08(08)	1.19(09)	7.72(08)	8.56(08)	$^2P_{3/2}$–$^2P_{3/2}$	8.25(08)	6.64(08)		3.75(09)
3–129	$2p^63p \leftarrow 2p^53p3d$	$^2P_{3/2}$–$^2P_{1/2}$	1.09(11)	6.00(10)	9.31(10)	7.97(10)	$^2P_{3/2}$–$^2S_{1/2}$	1.99(12)	1.60(12)		1.34(12)

		Ti^{11+}						Zn^{19+}				
i–j	Transitions	Terms	Present	FAC	Chen89	ZSC89[d]	SJS02	Terms	Present	FAC	ZSC89[b]	SJS02
1–6	$2p^63s \leftarrow 2p^53s^2$	$^2S_{1/2}$–$^2P_{3/2}$	2.71(11)	2.55(11)	2.50(11)	3.26(11)	3.25(11)	$^2S_{1/2}$–$^2P_{3/2}$	1.27(12)	1.36(12)	1.41(12)	1.65(12)
1–7	$2p^63s \leftarrow 2p^53s^2$	$^2S_{1/2}$–$^2P_{1/2}$	2.63(11)	2.59(11)	2.53(11)	3.44(11)	3.27(11)	$^2S_{1/2}$–$^2P_{1/2}$	1.21(12)	1.44(12)	1.62(12)	1.71(12)
1–38	$2p^63s \leftarrow 2p^53s3d$	$^2S_{1/2}$–$^4P_{1/2}$	9.01(09)	1.00(10)				$^2S_{1/2}$–$^4P_{1/2}$	4.76(10)	7.37(10)	1.69(11)	1.44(11)
1–39	$2p^63s \leftarrow 2p^53s3d$	$^2S_{1/2}$–$^4P_{3/2}$	2.50(10)	2.87(10)			1.84(10)	$^2S_{1/2}$–$^4P_{3/2}$	1.99(11)	1.83(11)	3.10(11)	3.96(11)
1–53	$2p^63s \leftarrow 2p^53s3d$	$^2S_{1/2}$–$^4D_{1/2}$	7.97(11)	8.64(11)			1.08(12)	$^2S_{1/2}$–$^2P_{1/2}$	3.41(12)	8.79(12)		9.68(12)
1–54	$2p^63s \leftarrow 2p^53s3d$	$^2S_{1/2}$–$^4D_{3/2}$	7.39(11)	9.42(11)		7.34(11)		$^2S_{1/2}$–$^2P_{3/2}$	6.29(12)	8.79(12)	1.26(13)	1.02(13)
2–8	$2p^63p \leftarrow 2p^53s3p$	$^2P_{1/2}$–$^4S_{3/2}$	1.01(09)	9.77(08)	9.75(08)		1.35(09)	$^2P_{1/2}$–$^4S_{3/2}$	8.36(08)	7.92(08)		4.01(08)
2–11	$2p^63p \leftarrow 2p^53s3p$	$^2P_{1/2}$–$^4D_{3/2}$	1.18(11)	1.15(11)	1.10(11)	1.55(11)	1.51(11)	$^2P_{1/2}$–$^2D_{3/2}$	1.12(12)	1.21(12)	1.31(12)	1.38(12)
2–12	$2p^63p \leftarrow 2p^53s3p$	$^2P_{1/2}$–$^4D_{1/2}$	9.94(10)	9.77(10)	1.13(11)	7.95(10)	1.60(11)	$^2P_{1/2}$–$^2P_{1/2}$	1.03(12)	1.11(12)	1.36(12)	1.48(12)
2–14	$2p^63p \leftarrow 2p^53s3p$	$^2P_{1/2}$–$^2D_{3/2}$	9.78(10)	8.97(10)	7.59(10)	9.57(10)	9.31(10)	$^2P_{1/2}$–$^2P_{3/2}$	2.31(11)	2.41(11)	2.03(11)	2.10(11)
2–15	$2p^63p \leftarrow 2p^53s3p$	$^2P_{1/2}$–$^4P_{1/2}$	1.80(10)	1.36(10)	1.32(10)	1.96(10)	1.30(10)	$^2P_{1/2}$–$^2S_{1/2}$	8.03(10)	8.61(10)	5.11(10)	4.35(10)
2–16	$2p^63p \leftarrow 2p^53s3p$	$^2P_{1/2}$–$^2P_{1/2}$	7.49(10)	6.86(10)	5.87(10)	1.93(11)	8.48(10)	$^2P_{1/2}$–$^4P_{1/2}$	5.96(11)	6.17(11)	7.30(11)	7.73(11)
2–17	$2p^63p \leftarrow 2p^53s3p$	$^2P_{1/2}$–$^4P_{3/2}$	1.54(11)	1.46(11)	1.30(11)	1.73(11)	1.70(11)	$^2P_{1/2}$–$^2P_{3/2}$	1.44(11)	1.84(11)	2.87(11)	2.51(11)
2–19	$2p^63p \leftarrow 2p^53s3p$	$^2P_{1/2}$–$^2P_{3/2}$	3.55(10)	3.35(10)	3.72(10)	5.47(10)	4.85(10)	$^2P_{1/2}$–$^4D_{3/2}$	9.67(11)	1.04(12)	1.18(12)	1.22(12)
2–22	$2p^63p \leftarrow 2p^53s3p$	$^2P_{1/2}$–$^2P_{3/2}$	1.18(11)	1.13(11)	1.26(11)	1.72(11)	1.53(11)	$^2P_{1/2}$–$^4P_{3/2}$	2.94(10)	2.92(10)	2.64(10)	4.38(10)
2–23	$2p^63p \leftarrow 2p^53s3p$	$^2P_{1/2}$–$^2P_{1/2}$	6.42(10)	5.55(10)	5.86(10)	5.54(10)	6.02(10)	$^2P_{1/2}$–$^2P_{1/2}$	4.60(09)	1.75(10)	5.38(10)	2.15(10)
3–83	$2p^63p \leftarrow 2p^53p3d$	$^2P_{3/2}$–$^4P_{1/2}$	5.09(10)	6.09(10)		2.56(10)	4.75(10)	$^2P_{3/2}$–$^4P_{1/2}$	6.52(11)	7.61(11)	3.05(11)	6.89(11)
3–107	$2p^63p \leftarrow 2p^53p3d$	$^2P_{3/2}$–$^2D_{5/2}$	2.64(11)	3.26(11)			1.94(11)	$^2P_{3/2}$–$^2D_{5/2}$	1.99(12)	2.47(12)		2.89(12)
3–120	$2p^63p \leftarrow 2p^53p3d$	$^2P_{3/2}$–$^2P_{3/2}$	5.18(10)	3.72(10)			5.99(10)	$^2P_{3/2}$–$^2P_{3/2}$	1.61(12)	1.38(12)		1.49(12)
3–129	$2p^63p \leftarrow 2p^53p3d$	$^2P_{3/2}$–$^2S_{1/2}$	8.70(12)	8.29(12)		5.31(12)	7.68(12)	$^2P_{3/2}$–$^2P_{1/2}$	4.08(13)	3.95(13)	2.16(13)	3.65(13)

[a] Refers to the work of Safronova *et al* [7] with relativistic many-body perturbation theory.
[b] Refers to the work of Safronova *et al* [7] with first-order perturbation theory.
[c] Refers to the work of Chen [19].
[d] Refers to the work of Zhang *et al* [8].
[e] (m) denotes $\times 10^m$.

here) can be included in the close-coupling expansion. But, the spectator Auger pathway dominates for $n > 3$. The last two channels, (3) and (4), represent radiation damping.

Our ICFT *R*-matrix calculations used a maximum of 25 continuum basis orbitals per orbital angular momentum over most of the sequence. This value is increased up to 60 continuum basis orbitals for Mg^+–Si^{3+} ions to avoid small oscillations in the high-energy collision strengths. Contributions from partial waves up to $J = 12$ were included in the exchange *R*-matrix calculation. The contribution from higher partial waves up to $J = 40$ were included via a non-exchange *R*-matrix calculation. A 'top-up' was used to complete the partial collision strength sum over higher *J*-values by using the [23] sum rule for dipole transitions and a geometric series for non-dipole transitions—see [24]. In the F-like iso-electronic sequence calculations, Witthoeft *et al* [13] repeated the calculation for some ions ($Z = 14$, 15, 20–22 and 28–30) with different energy meshes in order to check the convergence of the effective collision strengths (Υ) with respect to resonance resolutions—we adopt the recommended energy meshes of [13]; see table 4. In the case of Fe^{15+}, we have tested the convergence of Υ for outer-shell excitation and found the recommended of Witthoeft to be suitable. Beyond the resonance region, for the exchange calculation, an energy

Table 4. The energy meshes (in unit of q^2, residual charge of ion) used for each ion.

Mesh	Atomic number			
q^2 Ryd	12–14	15–21	22–30	31–36
1×10^{-4}	•			
5×10^{-5}		•		
1×10^{-5}			•	
5×10^{-6}				•

mesh of $0.01 \times q^2$ was used. For the non-exchange calculation, we used a step of $1 \times 10^{-3} q^2$ Ryd over the entire energy range. The *R*-matrix calculation was carried out up to an incident energy of 12 times the ionization potential for each ion. We then used the infinite energy Born limits (non-dipole allowed) and line-strengths (dipole-allowed) from AUTOSTRUCTURE so that higher energy reduced collision strengths, as defined by Burgess and Tully [25], can be found from interpolation in Burgess–Tully space for all additional higher energies. The effective collision strengths at 13 electron temperatures ranging from $2 \times 10^2 (q+1)^2$ K to $2 \times 10^6 (q+1)^2$ K (q is the residual charge of the ion, that is $Z - 11$) are produced as the end product. The data were stored in the ADAS adf04 format [26].

3. Results and discussions

3.1. Comparison with previous calculation for the core-excitations

We compare the present ICFT *R*-matrix results with those of previous works for three ions (Si^{3+}, Ca^{9+} and Kr^{25+}) which span the calculated data for this iso-electronic sequence. To the best of our knowledge, the only inner-shell *R*-matrix calculations available in the Na-like sequence are for Fe^{15+}. The work of Liang *et al* [12] reveals that the ICFT *R*-matrix calculation without damping shows good agreement with the DARC *R*-matrix results [11]. When Auger-plus-radiation damping is taken into account, the resonance enhancement for Υ is significantly reduced.

For Si^{3+} and Ca^{9+}, there are no Υ or original collision strength (Ω) data available to the best of our knowledge. So, for comparison purposes, we calculated the core-excitation data of Si^{3+} and Ca^{9+} using the FAC [20]. As shown in figures 5(a) and (b) for the $2p^6 3s^2 S_{1/2} \rightarrow 2p^5 3s 3p^2 S_{1/2}$ excitation, the FAC calculation agrees with the background collision strength in the present ICFT *R*-matrix calculation to within 15% for Si^{3+} and Ca^{9+}. The differences (between the FAC and present calculations) in low-temperature Maxwellian averaged effective collision strengths for these ions can be large due to resonant enhancement but (the expected) closer agreement is found at high temperatures.

Relativistic DW calculations were performed by Zhang *et al* [8] for Kr^{25+}. However, only Ω, at five scaled energies ranging from 1.0 to 15.0 (in threshold units) are available. As shown in figure 5(c), the background of the present ICFT Ω ($2p^6 3s^2 S_{1/2} \rightarrow 2p^5 3s 3p^2 S_{1/2}$ excitation) shows good agreement with the DW data of [8]. From Zhang *et al*'s Ω, we derived Υ and made comparison with the present results. The inset of figure 5(c) illustrates the comparison between the present ICFT *R*-matrix result and those from relativistic DW Ω of [8]. At low temperatures, a large difference (around a factor of 2) appears as could be expected—this is due

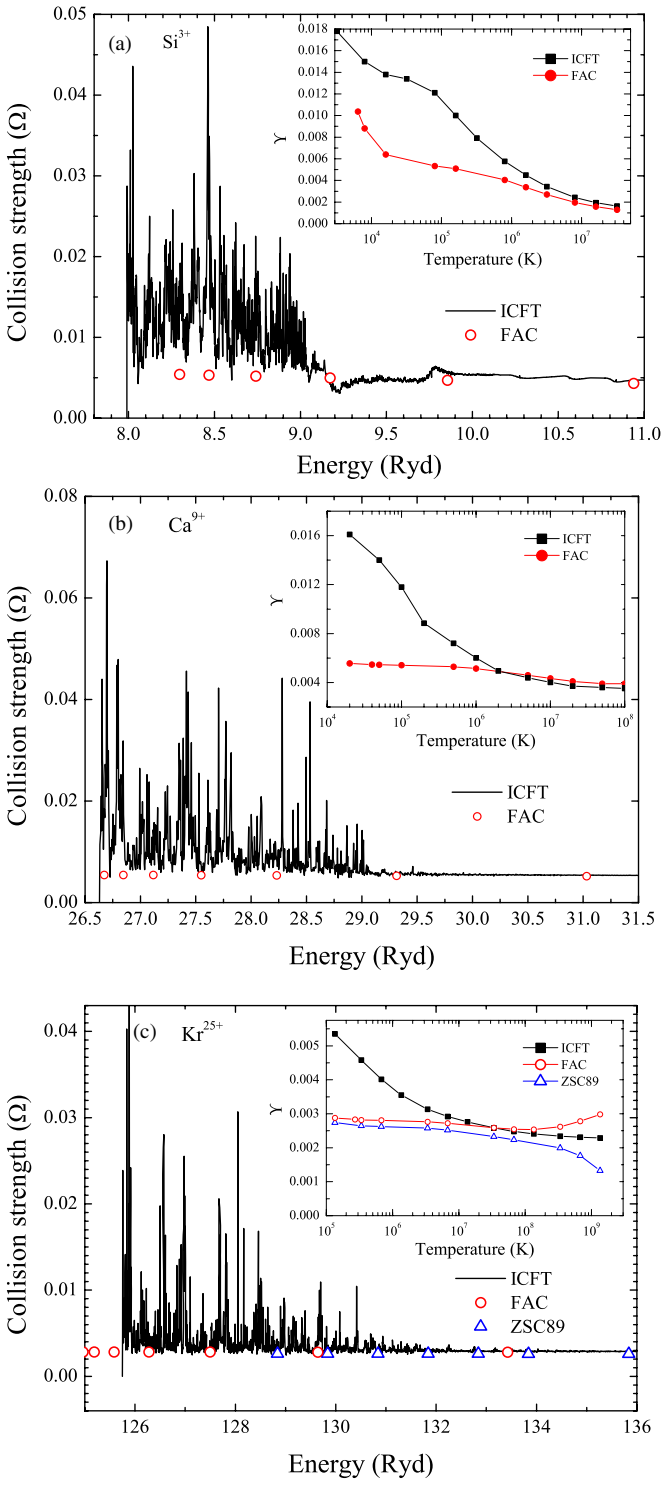

Figure 5. The comparison of the (effective) collision strength (inset) Ω for the $2p^6 3s^2 S_{1/2} \rightarrow 2p^5 3s 3p^2 S_{1/2}$ (1–15) excitation between the present ICFT *R*-matrix and previous available data. (a) Si^{3+}, FAC denotes the present DW calculation; (b) Ca^{9+} and (c) Kr^{25+}, ZSF89 refers to the work of Zhang *et al* [8].

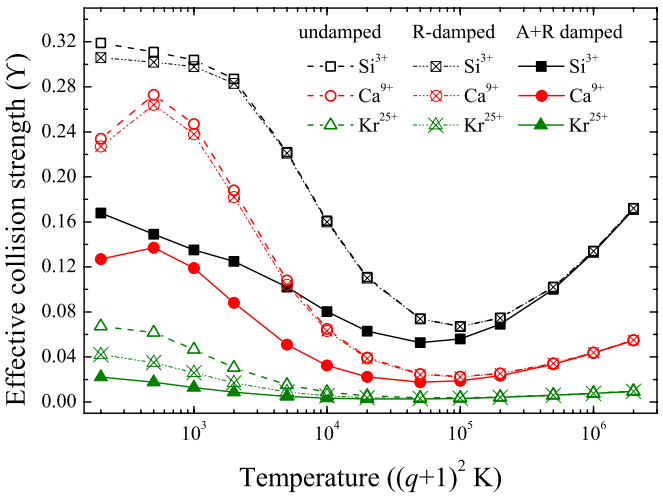

Figure 6. Comparison of the effective collision strength for the $2p^6 3s^2 S_{1/2} \rightarrow 2p^5 3s^2\ ^2P_{3/2}$ excitation (1–6) between the undamped, radiation (*R*-) damped and Auger-plus-radiation (A+R) damped ICFT *R*-matrix calculations for Si^{3+}, Ca^{9+} and Kr^{25+}.

to dense and strong resonances around the threshold in the present *R*-matrix calculations. With increasing temperature, the difference decreases as expected; however, it starts to enlarge again when $T_e > 1.0 \times 10^8$ K. This is simply because we assume, for the purposes of simplicity, a constant Ω value at high collision energies when we extrapolate the collision strength of Zhang *et al*'s data to the high-energy limit. The FAC calculation indicates that the collision strength increases again above an impact energy of $\sim 9.0 \times 10^3$ eV, which results in the FAC calculation being higher than the present calculation at $T_e > 1.0 \times 10^9$ K. The difference of radiative decay rates between them (FAC: 4.29×10^6 s^{-1} and AUTOSTRUCTURE: 1.73×10^6 s^{-1}) confirms that the deviation of Υ at high temperatures is due to large uncertainty of the underlying structure calculation for this weak transition.

3.2. *Damping effect along the sequence*

A detailed comparison between the damped and undamped Υ for Fe^{15+} has been made in our previous work [12] which showed that Auger-plus-radiation damping significantly reduces the resonance enhancement of the effective collision strengths by up to a factor 3 for some transitions. Here, we investigate the damping effect along the sequence via a detailed study of results for Si^{3+}, Ca^{9+} and Kr^{25+}. Figure 6 shows the effective collision strength for the $2p^6 3s^2 S_{1/2} \rightarrow 2p^5 3s^2\ ^2P_{3/2}$ excitation (1–6). They demonstrate that the Auger-plus-radiation damping decreases the resonance-enhanced Υ by 47%, 46% and 67% at $2 \times 10^2 (q+1)^2$ K for Si^{3+}, Ca^{9+} and Kr^{25+}, respectively. This indicates that the Auger-plus-radiation damping is more significant for higher charged ions.

The non-resonant contribution to an electron-impact excitation collision strength scales approximately as $1/Z^2$ while, in the absence of radiation damping, the resonant collision strength scales approximately as $1/Z^0$ [27]. That is the resonance-enhancement fractional contribution scales as $\frac{\Upsilon_{R,1}}{\Upsilon_{non,1}/Z^2+\Upsilon_{R,1}}$ (where $\Upsilon_{non,1}$ and $\Upsilon_{R,1}$ denote the non-resonant and the resonance enhancement in the hydrogen case). With increasing nuclear charge, the resonance contribution will become dominant until the radiation damping becomes significant and reduces the effect of resonances. Auger rates are independent of *Z* while radiation rates have a dependence of Z^4 for $\delta n > 0$ core transitions [28]. The radiation damping will lower the resonant cross-section and it is expected to be more significant for higher charge ions. Separate calculations, which only include radiation damping, have been performed for Si^{3+}, Ca^{9+} and Kr^{25+}. Figure 6 shows that the radiation damping lowers the resonance contribution to Υ about 4%, 3% and 38% for Si^{3+}, Ca^{9+} and Kr^{25+} at $2 \times 10^2 (q+1)^2$ K, respectively. The Auger damping effect is the dominant damping effect on the reduction of the resonance enhancement of Υ for lower charged ions. It still plays an important role in the reduction for higher charge ions, although the radiation damping increases significantly.

The widespread effect of Auger-plus-radiation damping is illustrated via a scatter plot of the ratios of damped to undamped Υ values for dipole transitions of ions Si^{3+} (figure 7(a)), Ca^{9+} (figure 7(c)) and Kr^{25+} (figure 7(e)) spanning the sequence. We see that the reduction from Auger and radiation damping at the low temperature $(2.0 \times 10^2 (q+1)^2$ K) can be up to a factor of 3 for a few dipole transitions of higher charge ions (e.g. <1% and 9% for Ca^{9+} and Kr^{25+}, respectively). For lower charge ions (e.g. Si^{3+}), the reduction is less than 40% for 99% dipole transitions. This confirms again that the Auger-plus radiation damping effect is stronger for higher charged ion. The effect decreases as expected with increasing temperature and is less than 10% for 95% (Si^{3+}), 90% (Ca^{9+}) and 83% (Kr^{25+}) of these transitions at high temperature $(1.0 \times 10^5 (q+1)^2$ K).

An illustrative way to quantify the information in the scatter plot is to count how many transitions differ by more than a given quantity. In figures 7(b), (d) and (f), we show the percentage of the dipole transitions where the damping effect is at least 5%, 10%, 15%, 20% and 30% for the three ions. 4%, 17% and 39% of dipole transitions show a damping effect of more than 30% at $2.0 \times 10^2 (q+1)^2$ K for Si^{3+}, Ca^{9+} and Kr^{25+}, respectively. At higher temperatures, the damping becomes weak and less widespread—1% (Si^{3+}), 7% (Ca^{9+}) and 16% (Kr^{25+}) of transitions are beyond 30% at $1.0 \times 10^4 (q+1)^2$ K. The percentage of higher charge ions, e.g. Kr^{25+}, is significantly higher than that of lower charge ions. This illustrates that the Auger-plus-radiation damping is more widespread for higher charge ions, as one would expect.

The widespread effect from radiation damping has also been explored for the three ions. There are about 100% (Si^{3+}), 99.8% (Ca^{9+}) and 92% (Kr25+) of dipole transitions showing a radiation damping effect less than 5% at $T_e = 2.0 \times 10^2 (q+1)^2$ K, which are significantly higher than that (68% for Si^{3+}; 35% for Ca^{9+} and 28% for Kr25+) with the Auger-plus-radiation damping included. This illustrates again that Auger damping is the dominant effect in the reduction of the resonance enhancement, and more widespread.

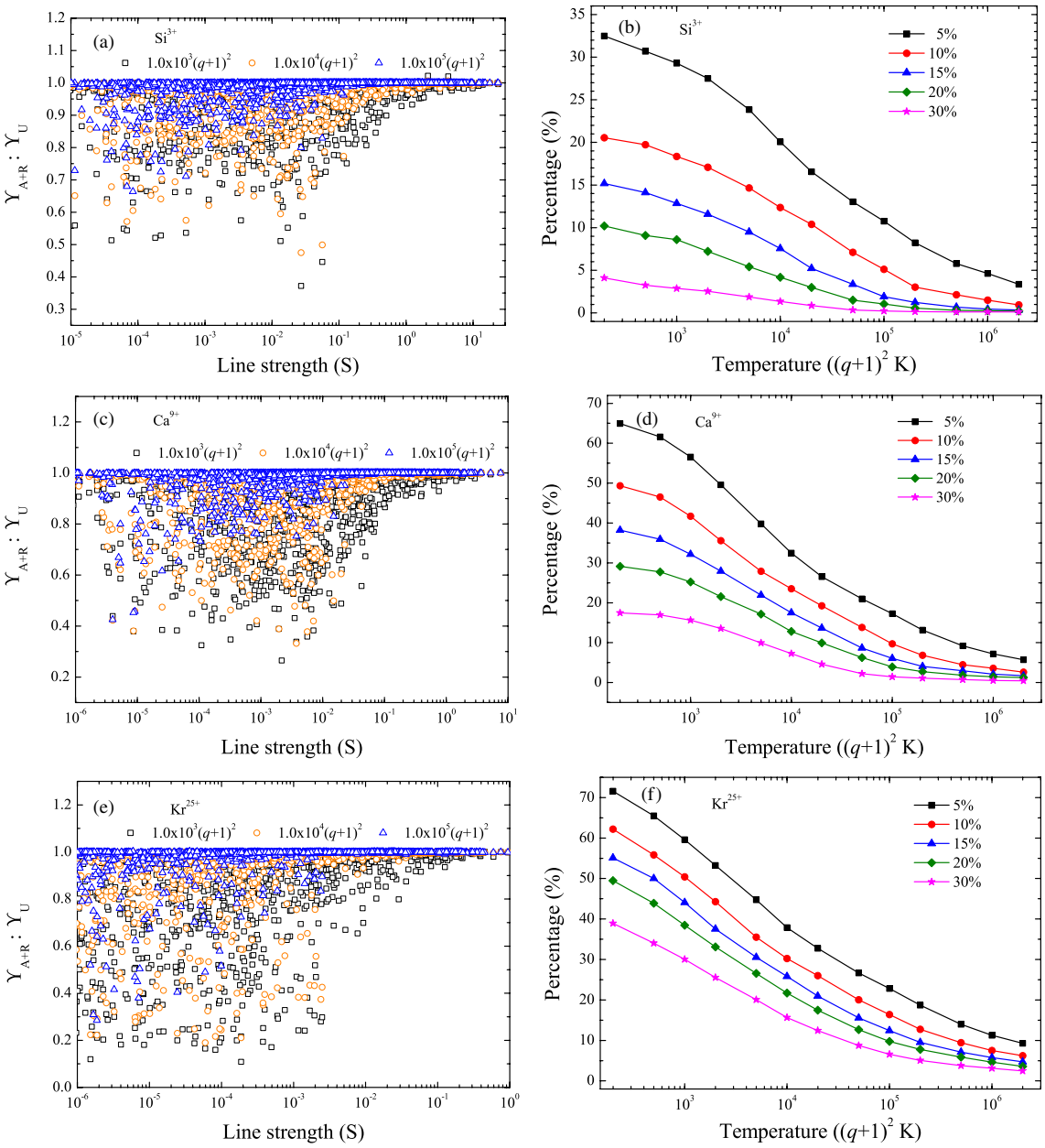

Figure 7. Left-hand panels: scatter plots showing the ratio of the effective collision strength (Υ) with Auger-plus-radiation damping (Υ_{A+R}) to without damping (Υ_U) as a function of line strength for dipole transitions of Si^{3+} (a), Ca^{9+} (c) and Kr^{25+} (e) at temperatures of $1.0 \times 10^{3,4,5}(q+1)^2$ K, where q is the ionic charge. Right-hand panels: percentage of the corresponding transitions where the effect of damping exceeds 5%, 10%, 15%, 20% and 30%.

3.3. Iso-electronic trends

As noted in the work of Witthoeft *et al* [13], the level mixing effect for higher excited levels strongly affects the behaviour of Υ along the sequence. In comparison with the transition decay rates explained in section 2.2, we also noted the sudden jumps of the $A_{i,j}$-value along the sequence for some transitions.

Although the Auger-plus-radiation damping significantly reduces the resonance contribution to the effective collision strength, the *R*-matrix Υ is still higher than the DW result (i.e. FAC calculations) by a factor of 2 at low temperature ($T_e = 10^2(q+1)^2$) for 58% of transitions to the five lowest-lying levels in Fe^{15+}. Thus, a complicated scaling of Υ along the iso-electronic sequence is to be expected here. In figure 8, we show Υ at $T_e = 10^3(q+1)^2$, $10^4(q+1)^2$ and $10^5(q+1)^2$ K for two inner-shell excitation transitions along the sequence: $2p^5 3s^2\ J = 3/2 \rightarrow 2p^6 3s\ J = 1/2$ (figure 8(a), dipole) and $2p^5 3s3p\ J = 5/2 \rightarrow 2p^6 3s\ J = 1/2$ (figure 8(b), non-dipole). At the low temperature $10^3(q+1)^2$ K, spikes and/or dips are observed along the iso-electronic sequence, which is completely different to that of the results of the DW calculation of [8, see figure 8]. Moreover, the present ICFT results are significantly higher than those from Zhang *et al*'s work. With increasing temperature, the spikes and/or dips disappear, as expected, because the resonance contribution becomes weaker and eventually negligible. As pointed out by Witthoeft *et al* [13], such spikes/dips along the iso-electronic

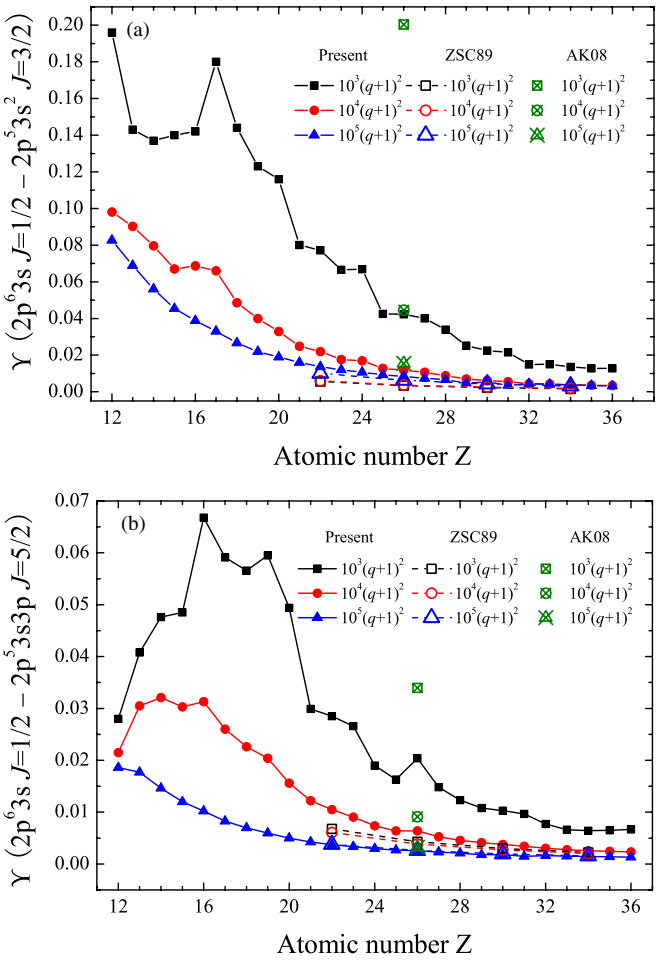

Figure 8. Effective collision strength (Υ) at temperatures of $T_e = 10^{3,4,5}(q+1)^2$ K along the iso-electronic sequence, and comparison with previous calculations in inner-shell transitions. AK08 denotes the work of Aggarwal and Keenan [11] for Fe^{15+}. (a) $2p^53s^2\ J = 3/2 \rightarrow 2p^63s\ J = 1/2$ dipole transition (1–6). (b) $2p^53s3p\ J = 5/2 \rightarrow 2p^63s\ J = 1/2$ non-dipole transition (1–9).

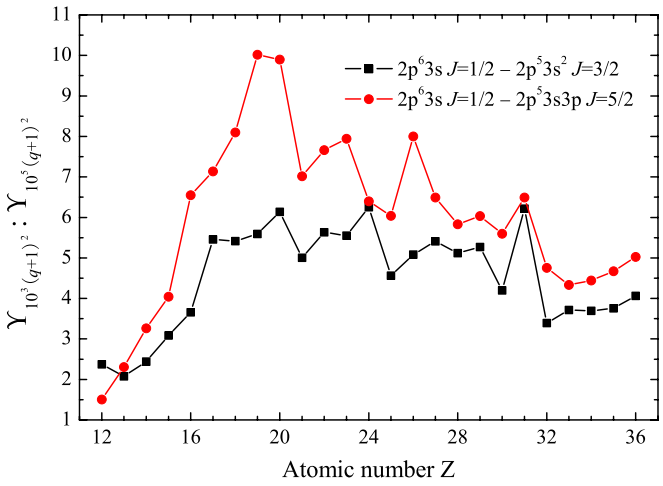

Figure 9. Effective collision strength (Υ) ratio between $T_e = 10^3(q+1)^2$ K and $T_e = 10^5(q+1)^2$ K along the iso-electronic sequence for $2p^53s^2\ J = 3/2 \rightarrow 2p^63s\ J = 1/2$ (1–6) and $2p^53s3p\ J = 5/2 \rightarrow 2p^63s\ J = 1/2$ (1–9) transitions.

sequence at low temperature are due to the steady shifting of groups of resonances down to, and below, threshold with increasing charge. The difference in results derived from Zhang *et al*'s work decreases with increasing T_e as would be expected.

The Υ-ratio along the sequence between the low ($10^3(q+1)^2$ K) and high ($10^5(q+1)^2$ K) temperatures clearly demonstrates that the complicated structure observed in Υ along the sequence is due to resonances (see figure 9). Moreover, their contribution to Υ reaches a maximum level around $17 \leqslant Z \leqslant 21$. The periodic spikes/dips in the Υ-ratio are more apparent for higher charged ions. This means that iso-electronic interpolations are not to be recommended.

4. Summary

We have performed 134-level ICFT *R*-matrix calculations for core-excitations of the Na-like iso-electronic sequence from Mg^+ to Kr^{25+}.

Good agreement with the results of others for level energies and gf/A-values (here g is the statistical weight of a given level, f and A are the oscillator strength and radiative decay rate for a given transition) for the iso-electronic sequence supports the reliability of the present *R*-matrix excitation data. This was confirmed specifically by detailed comparisons of Ω/Υ for Si^{3+}, Ca^{9+} and Kr^{25+}.

Poorer structure for ($Z = 12$–14) increases the uncertainty of our excitation data of these ions (Mg^+, Al^{2+} and Si^{3+}). A more elaborate *R*-matrix calculation, e.g. with pseudostates (RMPS), is necessary to test the present data here. This exceeds the scope of the present work. Similarly, fully relativistic calculations may be required for the upper end of the sequence ($Z = 34$–36). Though comparisons have been made for Si^{3+}, Ca^{9+} and Kr^{25+} confirming the background of the present ICFT *R*-matrix calculation, the data of [8] and the present FAC calculation do not consider resonance enhancement. For the rest of the sequence ($Z = 15$–33), the present excitation data are useful and reliable for spectroscopy/diagnostic research within the astrophysical and fusion communities. These data are made available through archives of APAP website (see footnote 1) in the ADAS adf04 format [26], ADAS[6] and CHIANTI[7].

The Auger-plus-radiation damping effect along the sequence was examined, it is significant and widespread over the entire sequence and more for higher charge ions. With increasing temperature, this effect becomes weaker and less widespread. The Auger damping effect was found to be dominant in the reduction of resonance enhancement on the electron-impact excitation over the entire sequence, though the radiation damping effect increases quickly with increasing nuclear charge.

By excluding the level mixing effects on Υ, we examined the iso-electronic trends of the effective collision strengths. A complicated pattern of spikes and dips of Υ at low temperatures was noted again along the sequence, which precludes interpolation in *Z*. With increasing temperature, the

[6] http://www.adas.ac.uk/.
[7] http://www.chianti.rl.ac.uk/.

difference between the present ICFT *R*-matrix and previous DW results decreases. It seems that resonance contribution to Υ quickly reaches the maximum level around $17 \leqslant Z \leqslant 21$.

In conclusion, we have generated an extensive set of reliable excitation data utilizing the ICFT *R*-matrix method. This will update the DW data presently used by the astronomical community and its use may overcome some shortcomings in the present astrophysical modelling, as seen in the cases of Mg IX [29] and Si X [30]. The Auger damping plays an important role in the reduction of resonance enhancement to the inner-shell electron-impact excitation over the iso-electronic sequence.

Acknowledgments

The work of the UK APAP Network is funded by the UK STFC under grant no. PP/E001254/1 with the University of Strathclyde. We would like to thank Professor U I Safronova for supplying data in electronic form as well as Dr M C Witthoeft and Dr C P Ballance for some helpful discussions.

References

[1] Behar E, Cottam J and Kahn S M 2001 *Astrophys. J.* **548** 966
[2] Jupén n C *et al* 1990 *Physica Scr.* **42** 44
[3] Brown G V, Beiersdorfer P, Chen H, Chen M H and Reed K J 2001 *Astrophys. J.* **557** L75
[4] Brown C M, Feldman U, Seely J F, Korendyke C M and Hara H 2008 *Astrophys. J. Suppl. Ser.* **176** 511
[5] Summers H P *et al* 2002 *Plasma Phys. Control. Fusion* **44** B323
[6] Safronova U I, Johnson W R, Safronova M S and Albritton J R 2002a *Phys. Rev.* A **66** 042506
[7] Safronova U I, Johnson W R, Safronova M S and Albritton J R 2002b *Phys. Rev.* A **66** 052511
[8] Zhang H L, Sampson D H, Clark R E H and Mann J B 1989 *At. Data Nucl. Data Tables* **41** 1
[9] Henry R J W and Msezane A Z 1982 *Phys. Rev.* A **26** 2545
[10] Tayal S S and Henry R J W 1989 *Phys. Rev.* A **39** 3890
[11] Aggarwal K M and Keenan F P 2008 *J. Phys. B: At. Mol. Opt. Phys.* **41** 015701
[12] Liang G Y, Whiteford A D and Badnell N R 2008 *J. Phys. B: At. Mol. Opt. Phys.* **41** 235203
[13] Witthoeft M C, Whiteford A D and Badnell N R 2007 *J. Phys. B: At. Mol. Opt. Phys.* **40** 2969
[14] Liang G Y, Whiteford A D and Badnell N R 2009a *Astron. Astrophys.* **500** 1263
[15] Griffin D C, Badnell N R and Pindzola M S 1998 *J. Phys. B: At. Mol. Opt. Phys.* **31** 3713
[16] Badnell N R 1986 *J. Phys. B: At. Mol. Opt. Phys.* **19** 3827
[17] Aggarwal K M and Keenan F P 2007 *Astron. Astrophys.* **463** 399
[18] Ralchenko Yu, Kramida A E and Reader J 2008 (NIST ASD Team) *NIST Atomic Spectra Database* (version 3.1.5) http://physics.nist.gov/asd3
[19] Chen M H 1989 *Phys. Rev.* A **40** 2365
[20] Gu M F 2008 *Can. J. Phys.* **86** 675
[21] Robicheaux F, Gorczyca T W, Pindzola M S and Badnell N R 1995 *Phys. Rev.* A **52** 1319
[22] Gorczyca T W and Robicheaux F 1999 *Phys. Rev.* A **60** 1216
[23] Burgess A 1974 *J. Phys. B: At. Mol. Phys.* **7** L364
[24] Badnell N R and Griffin D C 2001 *J. Phys. B: At. Mol. Opt. Phys.* **34** 681
[25] Burgess A and Tully J A 1992 *Astron. Astrophys.* **254** 436
[26] Summers H P 2004 *The ADAS User Manual* (version 2.6) http://www.adas.ac.uk/
[27] Seaton M J 1969 *J. Phys. B: At. Mol. Phys.* **2** 5
[28] Gorczyca T W, Robicheaux F, Pindzola M S and Badnell N R 1995 *Phys. Rev.* A **52** 3852
[29] Del Zanna G, Rozum I and Badnell N R 2008 *Astron. Astrophys.* **487** 1203
[30] Liang G Y, Whiteford A D and Badnell N R 2009b *Astron. Astrophys.* **499** 943